

# Shape-Induced Kinetics Enhancement in Layered P2-Na<sub>0.67</sub>Ni<sub>0.33</sub>Mn<sub>0.67</sub>O<sub>2</sub> Porous Microcuboids Enables High Energy/Power Sodium-Ion Full Battery

Bo Peng,<sup>[a]</sup> Zhihao Sun,<sup>[a]</sup> Liping Zhao,<sup>[a]</sup> Suyuan Zeng,<sup>[b]</sup> and Genqiang Zhang\*<sup>[a]</sup>

P2-type Na<sub>0.67</sub>Ni<sub>0.33</sub>Mn<sub>0.67</sub>O<sub>2</sub> cathode material generally suffers from poor cycling and rate performance due to fiercely phase variation and low Na<sup>+</sup> diffusion kinetic. Although efforts have been made to promote the electrochemical properties through ionic doping, the specific capacity reduction in most cases since the doped cations are electrochemical inactive cannot be neglected. Recently, some pioneering work have demonstrated that the advanced morphological design could significantly improve Na<sup>+</sup> intercalation kinetics. But rare researches devote to improving the electrochemical performance on P2-type Na<sub>0.67</sub>Ni<sub>0.33</sub>Mn<sub>0.67</sub>O<sub>2</sub> through morphological manipulation. Herein, unique one-dimensional P2-type Na<sub>0.67</sub>Ni<sub>0.33</sub>Mn<sub>0.67</sub>O<sub>2</sub> porous microcuboids with abundantly exposed {010} facets have been well designed via a simple one-pot strategy. Due to the reasonable material design, it demonstrates unprecedented electrochemical performances. Particularly, it can deliver high rate performance with 122.1 mAh g<sup>-1</sup> at 5 C, extraordinary cycle life with a capacity retention of 94.6% after 1500 cycles at 5 C. More importantly, prototype sodium ion full cell could achieve state-of-the-art power density of 1383.1 W kg<sup>-1</sup> with high energy density of 84.7 Wh kg<sup>-1</sup>. The underlying mechanism of enhanced electrochemical properties of this well-designed material has been deciphered through dynamic analysis, in-situ X-ray diffraction and structural analysis after cycling.

The unprecedented desire on sustainable energy utilization has intensively stimulated the development of large-scale electric energy storage (EES) devices in order to balance the electrical energy production between the peak and off-peak periods.<sup>[1,2]</sup> Recently, sodium-ion batteries (SIBs) have been considered as more suitable candidate for large-scale applications due to the abundance of sodium and much lower cost while comparable energy/power densities and analogue electrochemical kinetics

compared to that of lithium-ion batteries (LIBs).<sup>[3–7]</sup> Although the research on anode materials for SIBs has recently been flourishing,<sup>[8–13]</sup> the exploration on cathodes is much underdeveloped since these materials are generally composed of multi-component oxides, which brings much difficulty on designed synthesis and structural control. However, the performance of the cathode side plays the decisive role on the energy/power density of the SIBs, where much efforts should be devoted in order to push forward the advance of practical applications.<sup>[14–16]</sup>

Layered transition metal oxides (Na<sub>x</sub>TMO<sub>2</sub>, TM=Co, Fe, Ni, Mn, Cr, etc.) are considered as a class of the promising cathode candidates for SIBs due to their high theoretical capacity and facile synthesis process.<sup>[17–21]</sup> Among these materials, P2-type Na<sub>0.67</sub>Ni<sub>0.33</sub>Mn<sub>0.67</sub>O<sub>2</sub> has recently gained much attention owing to its high operating voltage ascribed to the high redox potential of Ni<sup>2+</sup>/Ni<sup>4+</sup> as well as attracting specific capacity.<sup>[22,23]</sup> However, the inevitable phase transition process and intrinsically sluggish Na<sup>+</sup> intercalation kinetics are prone to result in fast capacity decay and inferior rate performance, which severely hinders its practical applications. In order to tackle these challenges, chemical cation substitution has been proven to be an effective strategy that can promote the structural stability and boost the Na<sup>+</sup> interaction kinetics.<sup>[24–28]</sup> For examples, Zhou group<sup>[27]</sup> has improved the cycling stability through Na-site Mg doping in bulk P2-Na<sub>0.7</sub>Ni<sub>0.4</sub>Mn<sub>0.6</sub>O<sub>2</sub>. Wu and co-workers<sup>[28]</sup> significantly promoted the rate performance through enhancing Na<sup>+</sup> diffusion rate via Fe doping. However, the introduction of extra cations could decrease the specific capacity since the doped cations are electrochemical inactive in most cases.<sup>[29,30]</sup> Moreover, it could also increase the complexity and cost for the materials preparation. Some pioneer work have demonstrated that the advanced morphological design could significantly improve Na<sup>+</sup> intercalation kinetics.<sup>[31–38]</sup> Very recently, the Guo group<sup>[39]</sup> designed cathode material with the exposed {010} active facets by multiple-layer oriented stacking nanosheets in Na[Li<sub>0.05</sub>Ni<sub>0.3</sub>Mn<sub>0.5</sub>Cu<sub>0.1</sub>Mg<sub>0.05</sub>]O<sub>2</sub>, which largely enhanced the electrochemical performance. It can then be speculated that the advanced nanostructure with combined features of well exposed {010} planes and hierarchically porous architecture could further facilitate the Na<sup>+</sup> intercalation kinetics, which remains a great challenge to make such unique morphology for P2-type Na<sub>0.67</sub>Ni<sub>0.33</sub>Mn<sub>0.67</sub>O<sub>2</sub> due to lack of appropriate approaches.

Herein, we presented one-dimensional P2-type Na<sub>0.67</sub>Ni<sub>0.33</sub>Mn<sub>0.67</sub>O<sub>2</sub> porous microcuboids (denoted as P2-NNMO-PMCs) with abundantly exposed {010} facets via a simple one-

[a] B. Peng, Z. Sun, L. Zhao, Prof. G. Zhang  
Hefei National Laboratory for Physical Sciences at the Microscale  
CAS Key Laboratory of Materials for Energy Conversion  
Department of Materials Science and Engineering  
University of Science and Technology of China  
Hefei, Anhui 230026 China  
E-mail: gazzhangmse@ustc.edu.cn

[b] Dr. S. Zeng  
Department of Chemistry and Chemical Engineering  
Liaocheng University, Liaocheng, 252059, China

 Supporting information for this article is available on the WWW under  
<https://doi.org/10.1002/batt.202000226>

 An invited contribution to a joint Special Collection between  
ChemElectroChem and Batteries & Supercaps dedicated to research Beyond  
Lithium-Ion Batteries

pot strategy for the first time. Thanks to the unique structure, the P2-NNMO-PMCs cathode can achieve an unprecedented capacity retention rate of 94.6% after 1500 cycles at 1 C ( $1 \text{ C} = 170 \text{ mA g}^{-1}$ ) in the potential range of 2.0–4.0 V vs.  $\text{Na}^+/\text{Na}$ , which is superior compared to previous literatures. Impressively, even when evaluated within a wider potential range of 1.5–4.0 V (vs.  $\text{Na}^+/\text{Na}$ ), it can still maintain a remarkable capacity retention rate of 80.1% at 5 C after 300 cycles with a high specific capacity of  $165.9 \text{ mAh g}^{-1}$  at 0.1 C. More importantly, the sodium-ion full battery using P2-NNMO-PMCs cathode and hard carbon anode can achieve an outstanding energy/power density of  $173.8 \text{ Wh kg}^{-1}/26.3 \text{ W kg}^{-1}$  and exhibit inspiringly high power density of  $1383.1 \text{ W kg}^{-1}$  corresponding to a decent energy density of  $84.7 \text{ Wh kg}^{-1}$ . The possible origin of the enhanced performance is revealed by the quantitative transport kinetics analysis based on the Galvanostatic Intermittent Titration Technique (GITT) measurement. The charge compensation mechanism together with the reaction mechanism are also analyzed by in-situ X-ray diffraction (XRD) and X-ray photoelectron spectroscopy (XPS) characterizations.

The synthesis of P2-NNMO-PMCs is conducted via a scalable one-pot strategy based on co-precipitation method followed by simple calcination. Firstly, uniform metal oxalate mixture solid microcuboids are prepared by a facile co-precipitation process (details were provided in the Experimental Section of the Supporting Information). The final product can be obtained by calcination treatment of the metal oxalate mixture after the solvent evaporation with programmed conditions at 450 °C for 6 h and then 900 °C for 15 h with a heating rate of 2 °C min<sup>-1</sup> according to the thermogravimetric (TG) curve (Figure S1, Supporting Information). The morphological information and phase evolution process are observed through the field-emission scanning electron microscopy (FESEM), transmission electron microscopy (TEM) and X-ray diffraction (XRD) characterizations. Figure 1A and B show the typical morphology of the metal oxalate mixture solid microcuboids, where high uniformity with length of about 5 μm and width of about 1.1 μm can be confirmed. The XRD pattern (Figure S2) indicates that the mixture could contain both Ni<sub>0.33</sub>Mn<sub>0.67</sub>C<sub>2</sub>O<sub>4</sub> and NaHC<sub>2</sub>O<sub>4</sub>(H<sub>2</sub>O) phases, which is reasonable according to the synthesis procedures. The elemental mapping results (Fig-

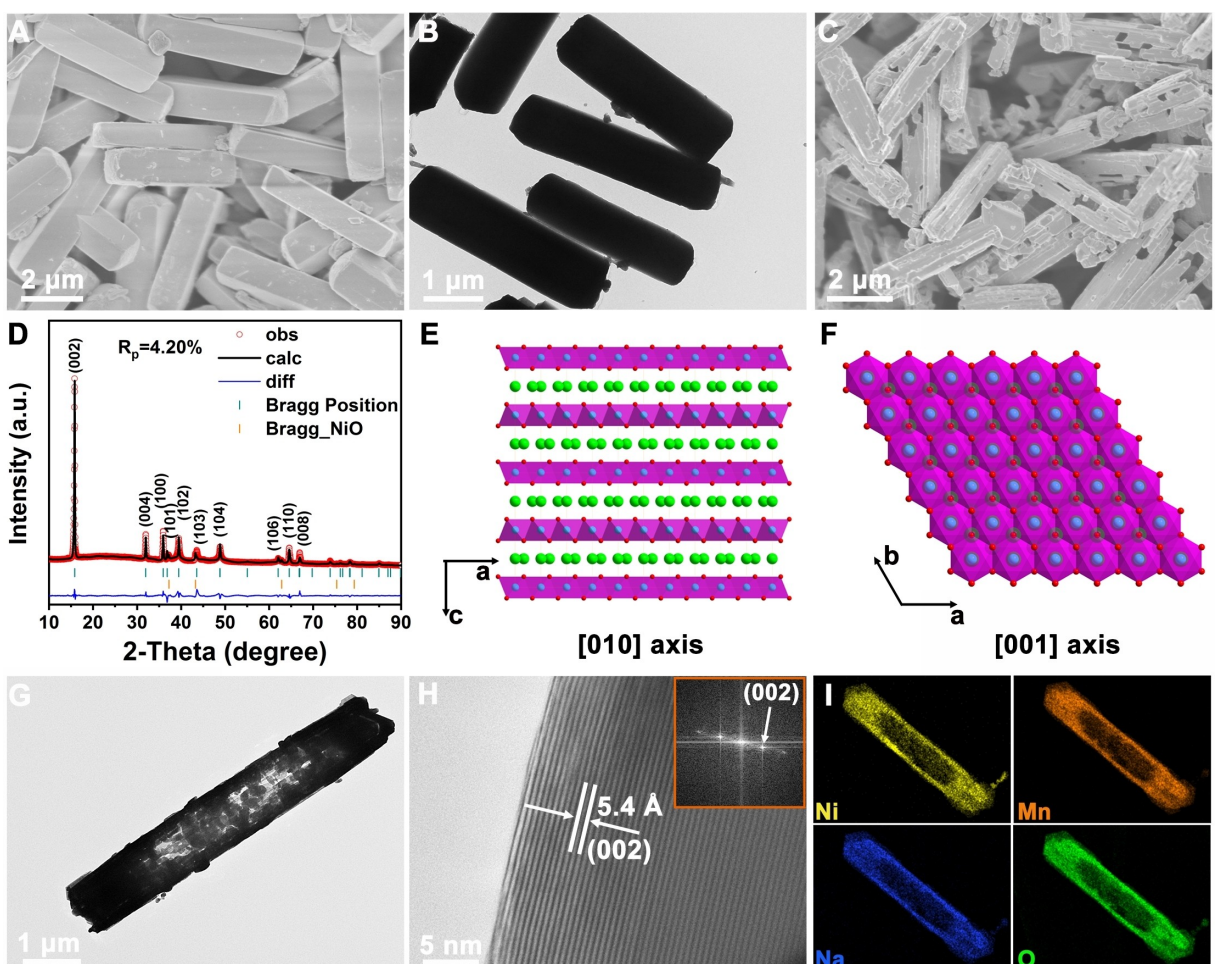


**Figure 1.** (A) FESEM and (B) TEM images of metal oxalate mixture solid microcuboids; (C–I): Characterizations of P2-NNMO-PMCs: (C) FESEM image, (D) Rietveld refinement of the XRD pattern for P2-NNMO-PMCs, (E, F) Corresponding crystal structure diagram. (G) TEM image, (H) HRTEM analysis and (I) Elemental mappings results. (Note: red spheres, blue spheres and green spheres in (E and F) represent O ions, metal ions (Ni, Mn) and Na ions, respectively).

ure S3) present the existence and uniform distributions of Na, Ni, Mn, C and O elements. After calcination, the 1D cuboid-like morphology can be mostly maintained, as shown in Figure 1C, while hierarchical pore structure can be clearly indicated due to the crystallization induced shrinkage and gaseous byproducts generation associated breakage. The XRD pattern of P2-NNMO-PMCs and the Rietveld refinement plots (Figure 1D) prove that P2-NNMMO-PMCs is indexed to hexagonal structure with a space group of  $P6_3/mmc$ , where alkali metal occupied prismatic sites between two  $MnO_2$  octahedral layers with oxygen atom formed ABBA series, as schematically illustrated in Figure 1E, F. The refined crystallographic parameters of P2-NNMO-PMCs are shown in Table S1. The typical TEM image (Figure 1G) further reveals the porous feature of P2-NNMO-PMCs with notable contrast difference. The high resolution TEM (HRTEM) analysis and corresponding fast Fourier transform (FFT) patterns taken from the randomly selected area (Figure 1H and Figure S4) indicate the good crystalline feature of the products. The clear lattice fringes with interplanar spacing of 5.4 Å can be readily ascribed to (002) planes, indicating the anisotropic growth direction of  $<001>$ . Importantly, the unique cuboid-like shape with highly porous structure will lead to the well expose of electrochemical active {010} facets, which could be beneficial to promote the  $Na^+$  intercalation kinetics. The composition of the P2-NNMO-PMCs is identified through energy dispersive X-ray spectroscopy (EDS), as shown in Figure S5, which is close to the stoichiometric ratios. The elemental mapping results (Figure 1I) indicate the uniform distribution of Ni, Mn, Na and O elements throughout the individual microcuboid. In addition, the X-ray photoelectron spectroscopy (XPS) measurement indicates the valance states of Ni and Mn in P2-NNMO-PMCs are +2 and +4 (Figure S6), respectively, which is consistent with previous literatures.<sup>[24,40]</sup> The bulk  $Na_{0.67}Ni_{0.33}Mn_{0.67}O_2$  (denoted as P2-NNMO-B) particles are synthesized via a conventional solid-state reaction as a control sample and its typical characterizations of phase, morphology and composites are provided in Figure S7, S8 and Table S2 (SI). The HRTEM analyses of P2-NNMO-B (Figure S9) indicate that there are no observable {010} planes in P2-NNMO-B, further suggesting the morphological effect of P2-NNMO-PMCs. The larger lattice parameter of  $c=11.1889\text{ \AA}$  in P2-NNMO-PMCs (Table S1) than that of P2-NNMO-B ( $c=11.1666$ , Table S2, SI) indicates the increased Na layer spacing, which could be beneficial for sodium ion diffusion. According to the calculated results from XRD patterns (Figure 1D and S7), the  $I_{(100)/(102)}$  value of P2-NNMO-PMCs (1.246) is about 1.96 times higher than that of P2-NNMO-B (0.636). This result obviously states the enhanced growth of the active {010} planes in porous microcuboids, which is consistent with the HRTEM result and previous reports.<sup>[41,42]</sup> In addition, the (100) plane has an open layered interspace for  $Na^+$  transport, but for the (102) plane, the atoms are densely packed and no clear access can be observed for  $Na^+$  transport, as depicted in the Figure S10. Therefore, the P2-NNMO-PMCs could induce fast sodium ion diffusion due to the exposed {010} facets.

The comparison investigation on the electrochemical performance of P2-NNMO-PMCs and P2-NNMO-B cathode is then conducted in a half cell configuration using Na metal as

counter electrode. The galvanostatic charge/discharge curves (Figure 2A) illustrate the higher specific capacity of  $85.4\text{ mAh g}^{-1}$  for P2-NNMO-PMCs than that of P2-NNMO-B ( $78.6\text{ mAh g}^{-1}$ ) tested at 1 C in the potential range of 2.0–4.0 V (1 C =  $170\text{ mA g}^{-1}$ ). The rate performances of P2-NNMO-PMCs and P2-NNMO-B are further investigated with the rate ranging from 0.1 to 10 C, as shown in Figure 2B and C, which can intuitively indicate the much better rate performance of the microcuboids, especially at high current rate. Specifically, an outstanding specific capacity of  $67.1\text{ mAh g}^{-1}$  can be maintained at 10 C and an unprecedented capacity retention of 77.5% from 0.1 to 10 C can be achieved, which is much higher than that of P2-NNMO-B ( $53.4\text{ mAh g}^{-1}$  at 10 C and a capacity retention of 61.1% from 0.1 to 10 C). The cycling performance of P2-NNMO-PMCs is demonstrated via long-term cycling measurement at 2 C and 5 C, as shown in Figure 2D and E, respectively. As depicted, it can deliver an initial specific capacity of  $83.2\text{ mAh g}^{-1}$  with a capacity retention of 98.3% after 300 cycles and could achieve a capacity retention of 94.6% after cycling 1500 cycles at 5 C. The cycling performance of P2-NNMO-PMCs is superior when compared with other reported layered oxide cathodes (Table S3).<sup>[19,24, 43–50]</sup> The calculated energy densities for P2-NNMO-PMCs electrode also exhibit an overwhelming advantage compared to P2-NNMO-B (Figure S11), which could be critical for full cell device. In addition, the testing potential range is further extended to 1.5–4.0 V to further investigate the effect of structural design on our P2-NNMO-PMCs. The galvanostatic charge/discharge curves (Figure S12) can intuitively indicate that the P2-NNMO-PMCs exhibit a higher specific capacity of  $165.9\text{ mAh g}^{-1}$  compared to that value of P2-NNMO-B ( $139.1\text{ mAh g}^{-1}$ ). The cyclic voltammetry (CV) profiles recorded at  $0.1\text{ mV s}^{-1}$  for the first four cycles (Figure S13) are well superposed with each other except the first cycle mainly due to the possible formation of SEI layer, implying the highly reversible electrochemical  $Na^+$  intercalation process for P2-NNMO-PMCs even within the broader potential range. Impressively, the P2-NNMO-PMCs still show a remarkable capacity retention rate of 44.7% from 0.1 C to 10 C, which is better than that value of P2-NNMO-B (22.6%), as shown in Figure 2F and Figure S14. The cycling stability of P2-NNMO-PMCs under 1.5–4.0 V is also outstanding, as shown in Figure 2G, which exhibits decent capacity retention of 80.1% after 300 cycles at 5 C with almost 100% coulombic efficiency. The comparison of the calculated energy densities within the potential range of 1.5–4.0 V (Figure S15) further illustrates the advantage of the unique shape induced performance enhancement for P2-NNMO-PMCs compared to P2-NNMO-B.

In order to decipher the possible origin for enhanced performance, the  $Na^+$  intercalation kinetics for P2-NNMO-PMCs and P2-NNMO-B are investigated based on the galvanostatic intermittent titration technique (GITT) measurement. It is generally accepted that the sodium ion diffusion coefficient ( $D_{Na^+}$ ) can be calculated by Equation (1) when the curve of typical  $E$  versus  $\tau^{1/2}$  profile present good linear relationship assuming that the diffusion of sodium ions in electrode materials follows Fick's second law<sup>[18,51]</sup>

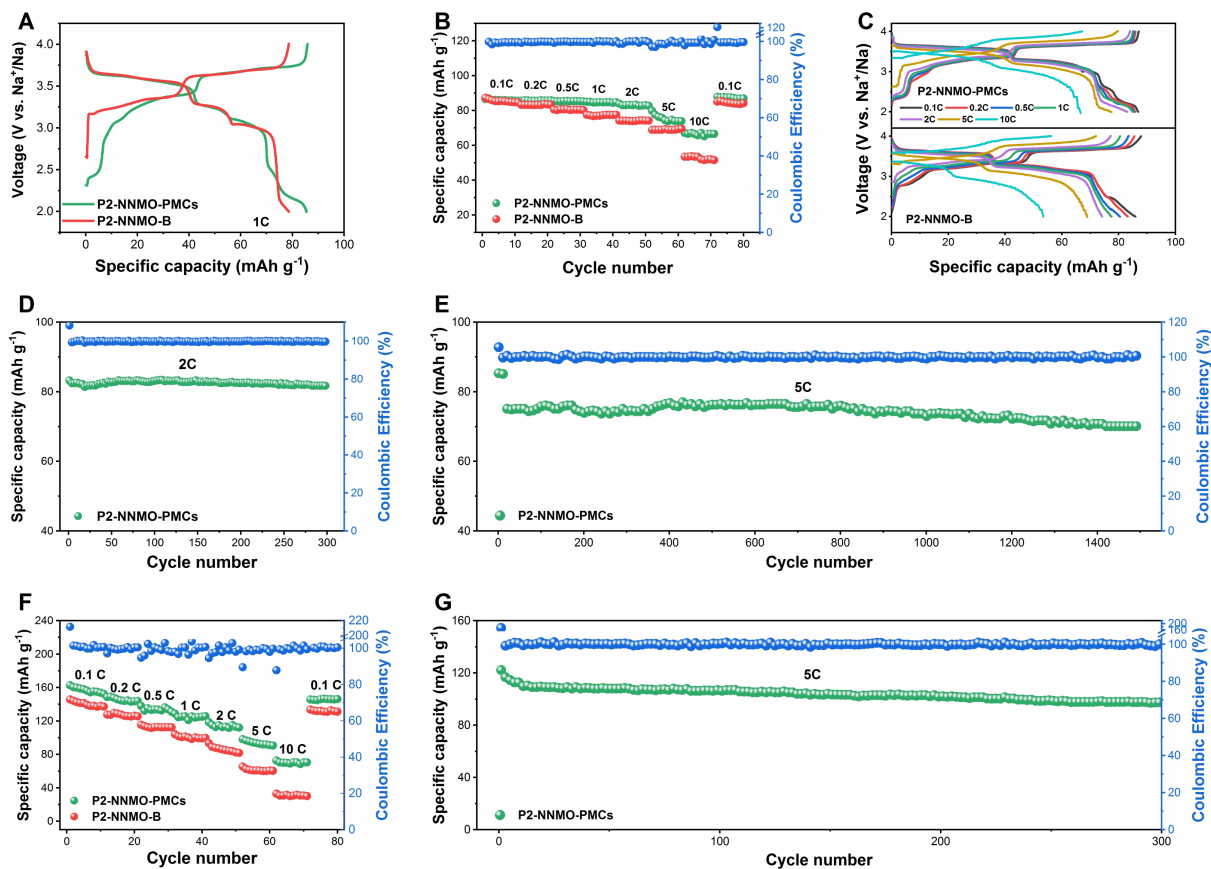


**Figure 2.** Electrochemical performance of P2-NNMO-PMCs cathode in a half cell configuration: (A) Charge-discharge curves at 1 C, (B) Rate performance and (C) corresponding charge-discharge curves for P2-NNMO-PMCs and P2-NNMO-B under 2.0–4.0 V; Cycling performance at (D) 2 C and (E) 5 C under 2.0–4.0 V; (F) The comparison study of the rate performance for P2-NNMO-PMCs and P2-NNMO-B under the potential range of 1.5–4.0 V; (G) Cycling performance of P2-NNMO-PMCs at 5 C rate under the potential range of 1.5–4.0 V.

$$D_{\text{Na}^+} = \frac{4}{\pi \tau} \left( \frac{m_B V_m}{M_B S} \right)^2 \left( \frac{\Delta E_s}{\Delta E_\tau} \right)^2, \tau \ll \frac{L^2}{D} \quad (1)$$

In which  $D_{\text{Na}^+}$  ( $\text{cm}^2 \text{s}^{-1}$ ) represents the  $\text{Na}^+$  diffusion coefficient in cathode,  $V_m$  ( $\text{cm}^3 \text{mol}^{-1}$ ),  $m_B$  and  $M_B$  mean the molar volume, weight and molar weight of the active material, respectively, and  $S$  is the surface area of the electrode ( $1.13 \text{ cm}^2$  in this work). The GITT charge/discharge curves (Figure 3A, B) with detailed parameters of  $\Delta E_s$  and  $\Delta E_\tau$  taken from a single step of the GITT (Figure 3C) can provide all the parameters to calculate the  $D_{\text{Na}^+}$  values. Because of the good linear relationship of  $E$  versus  $\tau^{1/2}$  curve (Figure 3D), the  $D_{\text{Na}^+}$  can be calculated through simplified formula of Equation (1). It can be notably observed (Figure 3E, F) that the average  $D_{\text{Na}^+}$  for P2-NNMO-PMCs is about  $1.6 \times 10^{-8} \text{ cm}^2 \text{s}^{-1}$ , which is about 8.2 times higher than that of P2-NNMO-B ( $1.94 \times 10^{-9} \text{ cm}^2 \text{s}^{-1}$ ), indicating more favorable  $\text{Na}^+$  intercalation kinetics in P2-NNMO-PMCs. In addition, the  $D_{\text{Na}^+}$  values calculated from multi-sweep CV profiles (Figure S16) give the consistent conclusion. The smaller polarizations of the redox couples in P2-NNMO-PMCs further prove the enhanced kinetics (Figure S17). The faster  $\text{Na}^+$  intercalation kinetics could be the major reason for the enhanced cycling stability and rate capability of P2-NNMO-PMCs. In addition, the electrochemical

impedance spectroscopy (EIS) measurement (Figure S18) shows smaller charge transfer impedance ( $R_{\text{ct}}$ ) of  $71.59 \Omega$  in P2-NNMO-PMCs than the value of  $113.3 \Omega$  in P2-NNMO-B (Table S4), which could be beneficial from the faster electron transfer process in 1D structure.<sup>[52]</sup> On the other hand, the combined analyses of P2-NNMO-PMCs after 100 cycles at 1C by XRD, FESEM and TEM characterizations (Figure S19) indicate that the phase, morphology and crystal structure can be well retained after repeated charge/discharge processes. In contrast, the P2-NNMO-B tends to crack after 100 cycles (Figure S20), which indicates the robust structure of the unique one-dimensional microcuboid morphology.

In order to further understand the  $\text{Na}^+$  storage mechanism, the charge compensation process is analyzed through ex situ X-ray photoelectron spectroscopy (XPS) results during the first charge/discharge process, as shown in Figure 4. As indicated, the peaks of  $\text{Ni } 2p_{3/2}$  and  $2p_{1/2}$  shift to higher bind energy at the charge state, which can reversibly return to pristine position when discharged to 1.5 V (Figure 4A). This phenomenon implies the reversible  $\text{Ni}^{2+}/\text{Ni}^{3+}$  redox couple during charge/discharge process.<sup>[53,54]</sup> In  $\text{Mn } 2p_{3/2}$  spectrum of the as prepared sample, as shown in Figure 4B, the deconvoluted peaks at 642.4 and 645 eV can be assigned to  $\text{Mn}^{4+}$  and  $\text{Mn}^{4+}$  satellite peak, respectively.<sup>[55–57]</sup> The valence of Mn-ions do not

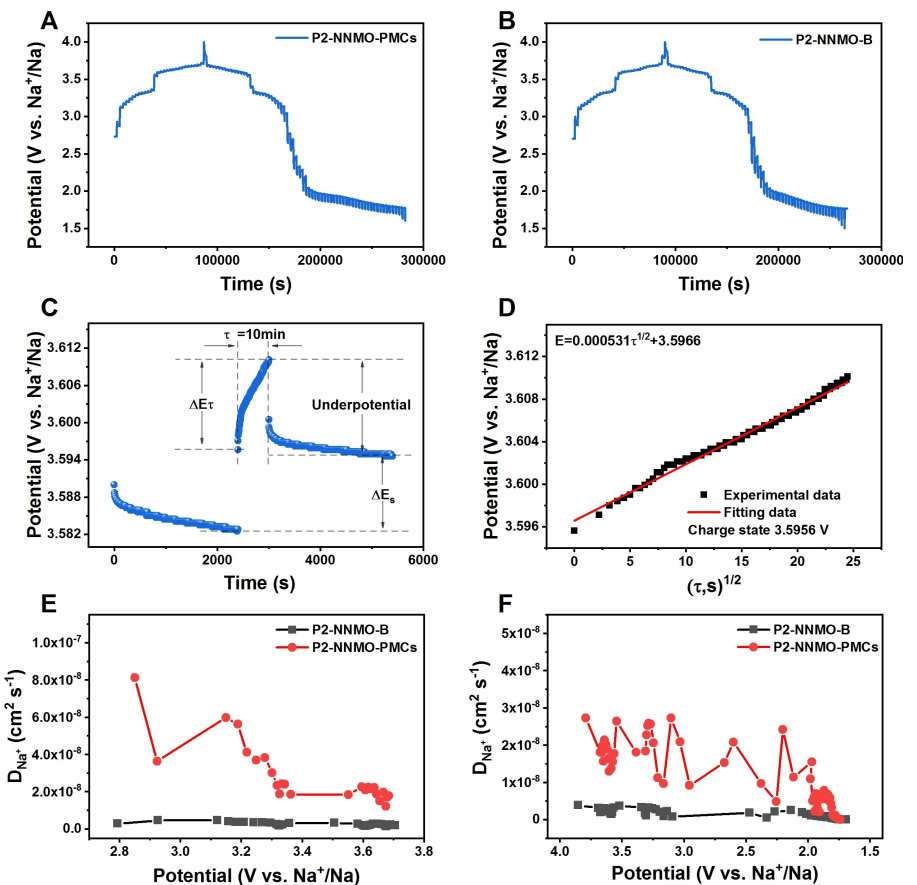


**Figure 3.** Kinetic characterization: GITT charge-discharge curves of (A) P2-NNMO-PMCs and (B) P2-NNMO-B; (C) A function of time in the potential range of 1.5–4.0 V for P2-NNMO-PMCs; (D) Liner behavior of the transient voltage changes  $E$  vs  $t^{1/2}$ ; (E, F) The calculated  $D_{\text{Na}^+}$  as a function of potential during charge and discharge process, for P2-NNMO-PMCs and P2-NNMO-B, respectively.

change during first charge process, while partial  $\text{Mn}^{4+}$  have been reduced to  $\text{Mn}^{3+}$  when the cathode discharged to 1.5 V, indicating that more  $\text{Na}^+$  are inserted back into host material due to the deficient reservoir of Na in  $\text{P2-Na}_{0.67}\text{Ni}_{0.33}\text{Mn}_{0.67}\text{O}_2$  phase.<sup>[58]</sup> Therefore, it can be concluded that 0.3 of  $\text{Na}^+$  can deintercalate from P2-NNMO-PMCs cathode per formula unit during first charge process through the oxidation of  $\text{Ni}^{2+}$  to  $\text{Ni}^{3+}$  for charge compensation. During the discharge process, 0.63 of  $\text{Na}^+$  can intercalate back into the host via reduction  $\text{Ni}^{3+}$  to  $\text{Ni}^{2+}$  and  $\text{Mn}^{4+}$  to  $\text{Mn}^{3+}$  for charge compensation. The phase evolution of P2-NNMO-PMCs electrode is further studied via *in-situ* XRD measurement, as shown in Figure 4C, D. As depicted, the P2-type structure can be well reserved during the charge/discharge process without any new emerging phase, indicating the stable crystal structure upon repeated cycles, which endows better cycling stability of P2-NNMO-PMCs. It should be noted that the position of the (002) peak gradually shifts to lower angle and (100) peak moves to higher angle during charge process, while both of them move to the opposite direction during discharge process (Figure 4D), which indicates reversible expansion and contraction of the lattice parameters, as shown in Figure S21. Note that the variations of cell volume after discharging to 1.5 V are much higher than 2.0 V, which could account for the much better cycling stability

in the voltage region of 2.0–4.0 V of P2-NNMO-PMCs. Based on the above analysis, the structural evolution process can then be schematically illustrated in Figure 4E, that is, the P2-type  $\text{Na}_{0.33}\text{Ni}_{0.33}\text{Mn}_{0.67}\text{O}_2$  can be generated at the charge state of 4.0 V accompanying with  $\text{Ni}^{2+}$  to  $\text{Ni}^{3+}$  transformation for charge compensation. At the discharge state of 1.5 V, P2-type  $\text{NaNi}_{0.33}\text{Mn}_{0.67}\text{O}_2$  with more sodium intercalation back is acquired coupled with  $\text{Ni}^{3+}$  to  $\text{Ni}^{2+}$  and  $\text{Mn}^{4+}$  to  $\text{Mn}^{3+}$  variations for charge compensation.

The practicability of P2-NNMO-PMCs cathode is preliminarily demonstrated by promising full cell performance assembled with P2-NNMO-PMCs as cathode and hard carbon as anode, as schematically illustrated in Figure 5A. The mass ratio between cathode and anode in full cell is carefully matched based on their electrochemical performance (Figure 5B and Figure S22). The rate performance of full cell is firstly measured, as shown in Figure 5C and D, where a high specific capacity of  $112.2 \text{ mAh g}^{-1}$  (based on cathode material) with a high initial coulombic efficiency of 74.6% tested at 0.1 C can be obtained. Importantly, the output voltages of the full cell (Figure S23) at different rate are quite stable ranging from 2.58 to 2.88 V, which exhibits great potential for high power devices. The corresponding Ragone plot (Figure 5E) is further calculated, where a remarkable energy density of  $173.8 \text{ Wh kg}^{-1}$  at a power

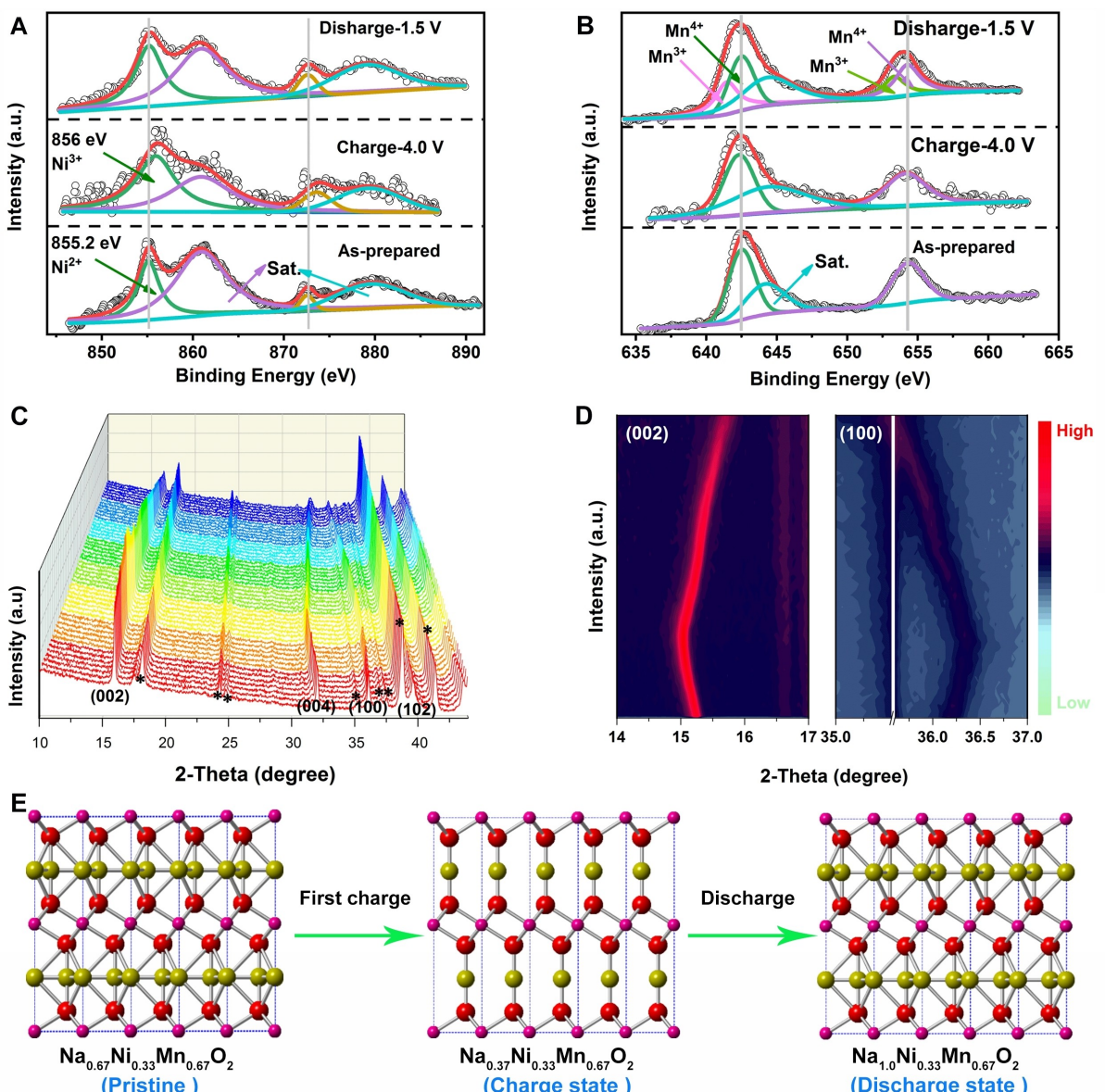


**Figure 4.** Sodium storage mechanism study of the P2-NNMO-PMCs. XPS of Ni 2p (A) and Mn2p (B) at different state; (C) In-situ XRD patterns of P2-NNMO-PMCs during first charge discharge process (note: the peaks labeled as black asterisks can be attributed to the in-situ XRD device and Al foil) and (D) corresponding contour maps of the main peaks of (002) and (100); (E) Schematic illustration showing 0.3  $\text{Na}^+$  deintercalating from  $\text{Na}_{0.67}\text{Ni}_{0.33}\text{Mn}_{0.67}\text{O}_2$  during the first charge process, and 0.63  $\text{Na}^+$  intercalating into the framework upon subsequent electrochemical discharge processes. (Note: red spheres, magenta spheres and dark yellow spheres in (E) represent O ions, metal ions (Ni, Mn) and Na ions, respectively).

density of  $26.3 \text{ W kg}^{-1}$  based on the total mass of both cathode and anode can be reached. More importantly, even at a high power density of  $1383.1 \text{ W kg}^{-1}$ , the P2-NNMO-PMCs cathode based full cell can still maintain an impressive energy density of  $84.7 \text{ Wh kg}^{-1}$ , demonstrating its great potential for high power devices. The full cell performance is highly competing when compared with recently reported state-of-the-art results (Table S5).<sup>[18,48, 59–66]</sup> In addition, the function of the full cell can be confirmed by powering the green LED logo (Inset in Figure 5E). Besides, the output voltage of the single full cell at charged state after relaxing for 2 h is measured to be as high as 3.73 V by multimeter (Figure S24A) and the brightness of powering LED (Figure S24B) implies the high energy/power

density. The full cell device also exhibits promising cycling stability as shown in Figure 5F, where a capacity retention of 69.6% after cycling 100 cycles at 1 C can be achieved. These results demonstrate the great potential for the P2-NNMO-PMCs as cathode candidates for SIBs.

In summary, we present a unique one-dimensional P2-type  $\text{Na}_{0.67}\text{Ni}_{0.33}\text{Mn}_{0.67}\text{O}_2$  porous microcuboids with abundantly exposed {010} facets for the first time as a promising cathode candidate for SIBs. Benefiting from the synergy of well exposed {010} facets and hierarchical porous structure, the P2-NNMO-PMCs cathode exhibits a superior capacity retention rate of 94.6% after 1500 cycles at 5 C in the potential range of 2.0–4.0 V (vs.  $\text{Na}^+/\text{Na}$ ). More inspiringly, even tested within a

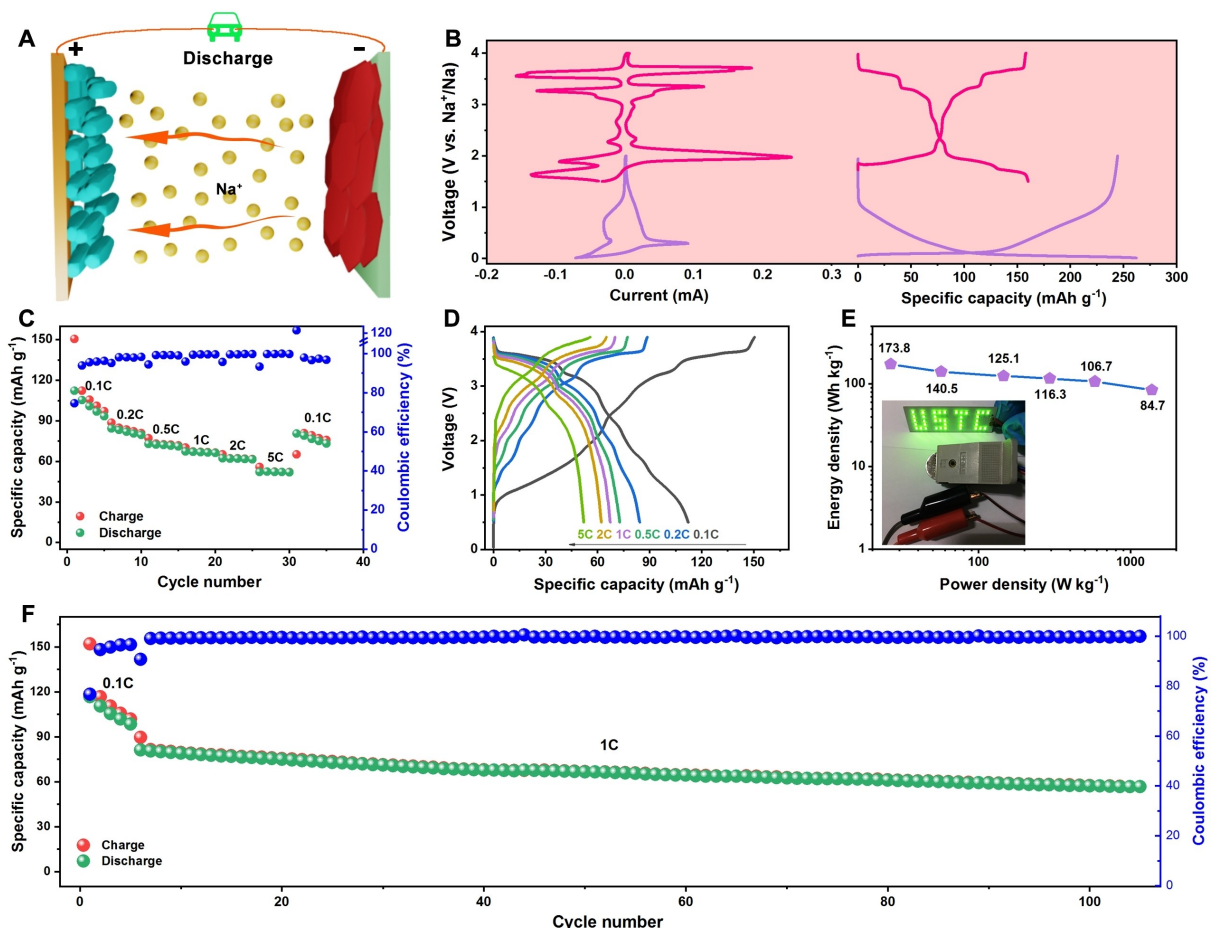


**Figure 5.** Full cell performance with P2-NNMO-PMCs and commercial hard carbon as cathode and anode, respectively. (A) Schematic illustration showing the discharge process; (B) CVs and charge/discharge curves of P2-NNMO-PMCs and hard carbon at  $0.1 \text{ mV s}^{-1}$ ,  $0.1 \text{ C}$  rate, respectively; (C, D) Rate performance; (E) Energy density vs. power density curve (inset, photo of powering the green LED "USTC" logo using single full cell); (F) Long term cycling performance at  $1 \text{ C}$  rate.

broader potential range of  $1.5\text{--}4.0 \text{ V}$  (vs.  $\text{Na}^+/\text{Na}$ ), it can not only deliver a high specific capacity of  $166 \text{ mAh g}^{-1}$  at  $0.1 \text{ C}$ , but also maintain an impressive capacity retention rate of  $80.1\%$  at  $5 \text{ C}$  after  $300$  cycles. The possible origin for the largely optimized performance and the storage mechanism are investigated by the combined analyses based on the Galvanostatic Intermittent Titration (GITT) measurement, in-situ X-ray diffraction (XRD) and X-ray photoelectron spectroscopy (XPS) characterizations. More importantly, the practicability of the P2-NNMO-PMCs is further demonstrated by assembling the sodium-ion full cell device, where an outstanding energy of  $173.8 \text{ Wh kg}^{-1}$  and a remarkable power density of  $1383.1 \text{ W kg}^{-1}$  corresponding to a decent energy density of  $84.7 \text{ Wh kg}^{-1}$  can be reached. This work not only provides a feasible route to boost  $\text{Na}^+$  intercalation kinetics, but also demonstrates the practicability of the P2-type layered oxide cathodes in SIBs for large-scale applications.

## Acknowledgements

G.Q.Z. acknowledges the financial support from the National Natural Science Foundation of China (Grant No. 51772284), the Recruitment Program of Global Experts and the Fundamental Research Funds for the Central Universities (WK2060000016). S.Y.Z. acknowledges the financial support from the Natural Science Foundation of Shandong Province (Grant No. ZR2016BQ41).

## Conflict of Interest

The authors declare no conflict of interest.

**Keywords:** sodium-ion full battery · layered transition metal oxide · cathode; porous microcuboid · high energy/power density

- [1] K. Zhang, D. Kim, Z. Hu, M. Park, G. Noh, Y. Yang, J. Zhang, V. W. Lau, S. L. Chou, M. Cho, S. Y. Choi, Y. M. Kang, *Nat. Commun.* **2019**, *10*, 5203.
- [2] H. Pan, Y.-S. Hu, L. Chen, *Energy Environ. Sci.* **2013**, *6*, 2338.

- [3] V. Palomares, P. Serras, I. Villaluenga, K. B. Hueso, J. Carretero-González, T. Rojo, *Energy Environ. Sci.* **2012**, *5*, 5884.
- [4] C. Delmas, *Adv. Energy Mater.* **2018**, *8*, 1703137.
- [5] B. Dunn, H. Kamath, J. M. Tarascon, *Science* **2011**, *334*, 928.
- [6] S. Chu, Y. Cui, N. Liu, *Nat. Mater.* **2016**, *16*, 16.
- [7] J. Y. Hwang, S. T. Myung, Y. K. Sun, *Chem. Soc. Rev.* **2017**, *46*, 3529.
- [8] S. H. Choi, Y. N. Ko, J.-K. Lee, Y. C. Kang, *Adv. Funct. Mater.* **2015**, *25*, 1780.
- [9] H. He, D. Huang, W. Pang, D. Sun, Q. Wang, Y. Tang, X. Ji, Z. Guo, H. Wang, *Adv. Mater.* **2018**, *30*, e1801013.
- [10] Z. Hu, Z. Tai, Q. Liu, S. W. Wang, H. Jin, S. Wang, W. Lai, M. Chen, L. Li, L. Chen, *Adv. Energy Mater.* **2019**, *9*, 1803210.
- [11] J. Gao, Y. Li, Y. Liu, S. Jiao, J. Li, G. Wang, S. Zeng, G. Zhang, *J. Mater. Chem. A* **2019**, *7*, 18828.
- [12] B. Li, Y. Liu, X. Jin, S. Jiao, G. Wang, B. Peng, S. Zeng, L. Shi, J. Li, G. Zhang, *Small* **2019**, *15*, 1902881.
- [13] Y. Xiao, J.-Y. Hwang, I. Belharouak, Y.-K. Sun, *Nano Energy* **2017**, *32*, 320.
- [14] P.-F. Wang, Y. You, Y.-X. Yin, Y.-G. Guo, *Adv. Energy Mater.* **2018**, *8*, 1701912.
- [15] Q. Liu, Z. Hu, M. Chen, C. Zou, H. Jin, S. Wang, S. L. Chou, S. X. Dou, *Small* **2019**, *15*, e1805381.
- [16] C. Vaalma, D. Buchholz, M. Weil, et al., *Nat. Rev. Mater.* **2018**, *3*, 18013.
- [17] L. Mu, S. Xu, Y. Li, Y. S. Hu, H. Li, L. Chen, X. Huang, *Adv. Mater.* **2015**, *27*, 6928.
- [18] B. Peng, Z. Sun, S. Jiao, J. Li, G. Wang, Y. Li, X. Jin, X. Wang, J. Li, G. Zhang, *J. Mater. Chem. A* **2019**, *7*, 13922.
- [19] J.-Y. Hwang, S.-T. Myung, C. S. Yoon, S.-S. Kim, D. Aurbach, Y.-K. Sun, *Adv. Funct. Mater.* **2016**, *26*, 8083.
- [20] J. Y. Hwang, J. Kim, T. Y. Yu, Y. K. Sun, *Adv. Energy Mater.* **2019**, *9*, 1803346.
- [21] T. Y. Yu, J. Y. Hwang, D. Aurbach, Y. K. Sun, *ACS Appl. Mater. Interfaces* **2017**, *9*, 44534.
- [22] G. Liu, L. Wen, Y. Li, Y. Kou, *Ionics* **2014**, *21*, 1011.
- [23] Z. Lu, J. R. Dahn, *J. Electrochem. Soc.* **2001**, *148*, A1225.
- [24] X. Wu, J. Guo, D. Wang, G. Zhong, M. J. McDonald, Y. Yang, *J. Power Sources* **2015**, *281*, 18.
- [25] P. F. Wang, Y. You, Y. X. Yin, Y. S. Wang, L. J. Wan, L. Gu, Y. G. Guo, *Angew. Chem. Int. Ed.* **2016**, *55*, 7445.
- [26] L. Wang, Y.-G. Sun, L.-L. Hu, J.-Y. Piao, J. Guo, A. Manthiram, J. Ma, A.-M. Cao, *J. Mater. Chem. A* **2017**, *5*, 8752.
- [27] Q. C. Wang, J. K. Meng, X. Y. Yue, Q. Q. Qiu, Y. Song, X. J. Wu, Z. W. Fu, Y. Y. Xia, Z. Shadike, J. Wu, X. Q. Yang, Y. N. Zhou, *J. Am. Chem. Soc.* **2018**, *141*, 840.
- [28] Q. Yang, P. F. Wang, J. Z. Guo, Z. M. Chen, W. L. Pang, K. C. Huang, Y. G. Guo, X. L. Wu, J. P. Zhang, *ACS Appl. Mater. Interfaces* **2018**, *10*, 34272.
- [29] G. Singh, N. Tapia-Ruiz, J. M. Lopez del Amo, U. Maitra, J. W. Somerville, A. R. Armstrong, J. Martinez de Illanduya, T. Rojo, P. G. Bruce, *Chem. Mater.* **2016**, *28*, 5087.
- [30] J. W. Somerville, A. Sobkowiak, N. Tapia-Ruiz, J. Billaud, J. G. Lozano, R. A. House, L. C. Gallington, T. Ericsson, L. Häggström, M. R. Roberts, U. Maitra, P. G. Bruce, *Energy Environ. Sci.* **2019**, *12*, 2223.
- [31] Y. Xiao, X. D. Zhang, Y. F. Zhu, P. F. Wang, Y. X. Yin, X. Yang, J. L. Shi, J. Liu, H. Li, X. D. Guo, B. H. Zhong, Y. G. Guo, *Adv. Sci.* **2019**, *6*, 1801908.
- [32] Y. L. T. J. S. Chen, C. M. Li, Y. L. Cheah, D. Luan, S. Madhavi, F. Y. Boey, L. A. Archer, X. W. Lou, *J. Am. Chem. Soc.* **2010**, *132*, 6124.
- [33] W. Ren, Z. Zheng, C. Xu, C. Niu, Q. Wei, Q. An, K. Zhao, M. Yan, M. Qin, L. Mai, *Nano Energy* **2016**, *25*, 145.
- [34] X. Zhang, F. Cheng, J. Yang, J. Chen, *Nano Lett.* **2013**, *13*, 2822.
- [35] H. Xia, X. Zhu, J. Liu, Q. Liu, S. Lan, Q. Zhang, X. Liu, J. K. Seo, T. Chen, L. Gu, Y. S. Meng, *Nat. Commun.* **2018**, *9*, 5100.
- [36] Y. Qi, Z. Tong, J. Zhao, L. Ma, T. Wu, H. Liu, C. Yang, J. Lu, Y.-S. Hu, *Joule* **2018**, *2*, 2348.
- [37] K. T. Kim, G. Ali, K. Y. Chung, C. S. Yoon, H. Yashiro, Y. K. Sun, J. Lu, K. Amine, S. T. Myung, *Nano Lett.* **2014**, *14*, 416.
- [38] B. Peng, Y. Li, J. Gao, F. Zhang, J. Li, G. Zhang, *J. Power Sources* **2019**, *437*, 226913.
- [39] Y. Xiao, P. F. Wang, Y. X. Yin, Y. F. Zhu, Y. B. Niu, X. D. Zhang, J. Zhang, X. Yu, X. D. Guo, B. H. Zhong, Y. G. Guo, *Adv. Mater.* **2018**, *30*, 1803765.
- [40] H. R. Yao, P. F. Wang, Y. Gong, J. Zhang, X. Yu, L. Gu, C. OuYang, Y. X. Yin, E. Hu, X. Q. Yang, E. Stavitski, Y. G. Guo, L. J. Wan, *J. Am. Chem. Soc.* **2017**, *139*, 8440.
- [41] Y. Li, Y. Bai, C. Wu, J. Qian, G. Chen, L. Liu, H. Wang, X. Zhou, F. Wu, *J. Mater. Chem. A* **2016**, *4*, 5942.
- [42] L. Zhang, N. Li, B. Wu, H. Xu, L. Wang, X. Q. Yang, F. Wu, *Nano Lett.* **2015**, *15*, 656.
- [43] D. Tie, G. Gao, F. Xia, R. Yue, Q. Wang, R. Qi, B. Wang, Y. Zhao, *ACS Appl. Mater. Interfaces* **2019**, *11*, 6978.
- [44] F. J. García-García, R. Klee, P. Lavela, M. R. D. Bomio, J. L. Tirado, *ChemElectroChem* **2020**, *7*, 3528.
- [45] Q. S. Yong Li, X. Yin, J. Wang, J. Wang, Y. Zhao, J. Zhang, *Chem. Eng. J.* **2020**, *402*, 126181.
- [46] K. Wang, H. Wan, P. Yan, X. Chen, J. Fu, Z. Liu, H. Deng, F. Gao, M. Sui, *Adv. Mater.* **2019**, *31*, 1904816.
- [47] T. Jin, P. F. Wang, Q. C. Wang, K. Zhu, T. Deng, J. Zhang, W. Zhang, X. Q. Yang, L. Jiao, C. Wang, *Angew. Chem. Int. Ed.* **2020**, *132*, 14619.
- [48] B. Peng, Z. Sun, S. Jiao, G. Wang, G. Zhang, *Batteries & Supercaps* **2020**, *3*, 147; *Supercaps* **2020**, *3*, 147.
- [49] I. Hasa, D. Buchholz, S. Passerini, B. Scrosati, J. Hassoun, *Adv. Energy Mater.* **2014**, *4*, 1400083.
- [50] S. Guo, P. Liu, H. Yu, Y. Zhu, M. Chen, M. Ishida, H. Zhou, *Angew. Chem. Int. Ed.* **2015**, *54*, 5894.
- [51] Z. Yan, L. Tang, Y. Huang, W. Hua, Y. Wang, R. Liu, Q. Gu, S. Indris, S. L. Chou, Y. Huang, M. Wu, S. X. Dou, *Angew. Chem. Int. Ed.* **2019**, *58*, 1412.
- [52] T. Jin, Q. Han, Y. Wang, L. Jiao, *Small* **2018**, *14*, 1703086.
- [53] K. Hemalatha, M. Jayakumar, P. Bera, A. S. Prakash, *J. Mater. Chem. A* **2015**, *3*, 20908.
- [54] Q. Li, Y. Qiao, S. Guo, K. Jiang, Q. Li, J. Wu, H. Zhou, *Joule* **2018**, *2*, 1134.
- [55] Y. Guo, Y. Tong, P. Chen, K. Xu, J. Zhao, Y. Lin, W. Chu, Z. Peng, C. Wu, Y. Xie, *Adv. Mater.* **2015**, *27*, 5989.
- [56] S. Li, S. Wang, Y. Lu, C. Zhang, X. Yang, J. Gao, D. Li, Y. Zhu, W. Liu, *AIP Adv.* **2018**, *8*, 015009.
- [57] R. Mohan, A. Modak, P. Subramanian, R. Cahan, P. Sivakumar, A. Gedanken, A. Schechter, *ChemElectroChem* **2020**, *7*, 561.
- [58] X. Bai, M. Sathiya, B. Mendoza-Sánchez, A. Iadecola, J. Vergnet, R. Dedryvère, M. Saubanère, A. M. Abakumov, P. Rozier, J.-M. Tarascon, *Adv. Energy Mater.* **2018**, *8*, 1802379.
- [59] D. Y. Yu, P. V. Prikhodchenko, C. W. Mason, S. K. Batabyal, J. Gun, S. Sladkevich, A. G. Medvedev, O. Lev, *Nat. Commun.* **2013**, *4*, 2922.
- [60] N. Wang, Z. Bai, Y. Qian, J. Yang, *Adv. Mater.* **2016**, *28*, 4126.
- [61] W. Duan, Z. Zhu, H. Li, Z. Hu, K. Zhang, F. Cheng, J. Chen, *J. Mater. Chem. A* **2014**, *2*, 8668.
- [62] S. Guo, P. Liu, Y. Sun, K. Zhu, J. Yi, M. Chen, M. Ishida, H. Zhou, *Angew. Chem. Int. Ed.* **2015**, *54*, 11867.
- [63] M. Fan, Y. Chen, Y. Xie, T. Yang, X. Shen, N. Xu, H. Yu, C. Yan, *Adv. Funct. Mater.* **2016**, *26*, 5019.
- [64] Y. Fang, L. Xiao, J. Qian, Y. Cao, X. Ai, Y. Huang, H. Yang, *Adv. Energy Mater.* **2016**, *6*, 1502197.
- [65] Y. Wang, R. Xiao, Y. S. Hu, M. Avdeev, L. Chen, *Nat. Commun.* **2015**, *6*, 6954.
- [66] B. Peng, J. Gao, Z. Sun, J. Li, G. Zhang, *J. Physics D: Applied Physics* **2020**, *54*, 014001.

Manuscript received: September 25, 2020

Revised manuscript received: November 26, 2020

Version of record online: December 10, 2020